Chemical and Resistive Switching Properties of Elaeodendron Buchananii Extract-Carboxymethyl Cellulose Composite: A Potential Active Layer for Biodegradable Memory Devices

Z.W. Dlamini

zdlamini@cut.ac.za

Central University of Technology

S. Vallabhapurapu

University of South Africa

J. Nambooze

University of Free State

E. Erasmus

University of Free State

R. Mogale

University of Free State

A. Wilhelm

University of Free State

MR. Swart

University of Free State

VS. Vallabhapurapu

University of South Africa

B. Mamba

University of South Africa

W. Seltalentoa

Central University of Technology

TS. Mahule

University of South Africa

VOL. Pellegrini

University of S˜ao Paulo

I. Polikarpov

University of S˜ao Paulo

Research Article

Keywords: Resistive switching memory, organic functional material, carboxymethyl cellulose, plant extract

Posted Date: March 19th, 2024

DOI: https://doi.org/10.21203/rs.3.rs-4121284/v1

Additional Declarations:
The authors declare no competing interests.

Supplementary Information is not available with this version.

Chemical and Resistive Switching Properties of *Elaeodendron* Buchananii Extract-Carboxymethyl Cellulose Composite: A Potential Active Layer for Biodegradable Memory Devices

Zolile Wiseman Dlamini[1*], Sreedevi Vallabhapurapu[2†], Jennifer Nambooze[3†], Anke Wilhelm[3†], Elizabeth Erasmus[3†], Refilwe Mogale[3†], Marthinus Rudi Swart[3†], Vijaya Srinivasu Vallabhapurapu[4†], Bheki Mamba[5†], Wendy Setlalentoa[1†], Tebogo Sfiso Mahule[4†], Vanessa de Oliveira Arnoldi Pellegrini [6†], Igor Polikarpov[6†]

[1*]Maths, Science and Technology Education, Central University of Technology, 20 President Brand Street, Bloemfontein, 9300, Free State, South Africa.
[2]School of Computing, University of South Africa, 28 Pioneer Avenue, Florida Park, 1710, Gauteng, South Africa.
[3]Chemistry Department, University of Free State, Nelson Mandela Drive, Bloemfontein, 9300, Free State, South Africa.
[4]Physics Department, University of South Africa, 28 Pioneer Avenue, Florida Park, 1710, Gauteng, South Africa.
[5]Institute for Nanotechnology and Water Sustainability, University of South Africa, 28 Pioneer Avenue, Florida Park, 1710, Gauteng, South Africa.
[6]São Carlos Institute of Physics, University of São Paulo, Jardim Santa Angelina, São Carlos, 13560-000, São Paulo, Brazil.

*Corresponding author(s). E-mail(s): zdlamini@cut.ac.za;
Contributing authors: vallas@unisa.ac.za; n.jennifer33@gmail.com; wilhelma@ufs.ac.za; erasmuse@ufs.ac.za; mogaler@ufs.ac.za; swartmr@ufs.ac.za; vallavs@unisa.ac.za; mambabb@unisa.ac.za; wsetlale@cut.ac.za; mahults@unisa.ac.za; varnoldi@yahoo.com.br; ipolikarpov@ifsc.usp.br;
†These authors contributed equally to this work.

Abstract

Biodegradable electronic devices play a crucial role in addressing the escalating issue of electronic waste accumulation, which poses significant environmental threats. In this investigation, we explored the utilization of a methanol-based extract of the *Elaeodendron buchananii* plant blended with carboxymethyl cellulose, a biopolymer, to produce a biodegradable and environmentally friendly functional material for a resistive switching memory system using silver and tungsten electrodes. Our analyses revealed that these two materials chemically interacted to generate a perfect composite with near semiconducting optical bandgap (**4.01** $\boldsymbol{eV}$), surpassing than that of individual materials. The resultant device exhibited O-type memory behavior, with a low ON/OFF ratio, strong endurance ($\geq$ $\mathbf{10^3}$ write/erase

cycles), and satisfactory ($\geq$ $\mathbf{10^3}$) data retention. Furthermore through a comprehensive transport mechanism analysis , we observed the formation of traps in the composite significantly improved conduction in the device. In addition, we established that altering the voltage amplitude modifies the concentration of traps, leading in voltage amplitude driven multiple resistance states. Overall, our findings underscore the potential of functionalizing polymers can be functionalized by incorporating plant extracts, thereby resulting in biodegradable nonvolatile memory devices with promising performance metrics.

Keywords: Resistive switching memory, organic functional material, carboxymethyl cellulose, plant extract

1 Introduction

Functionalization of materials stands as a pivotal strategy in advancing the frontiers of contemporary science and technology. Functional materials can be carefully engineered to possess precise properties or functions that can be tailored for a wide range of uses[1–3]. These materials have the ability to display properties like higher conductivity, increased strength, or enhanced reactivity, making them valuable in various applications such as electronics, energy storage, information technology, catalysis, and more[2]. Through the process of functionalizing materials, researchers and engineers have the ability to tap into the complete capabilities of these materials, leading to the development of groundbreaking solutions for a wide range of complex problems across various applications. Functional materials, such as organic composites, have become increasingly important in enhancing the capabilities of modern electronics. Organic composites, comprising a blend of organic polymers and other substances, offer unique advantages in terms of their flexibility, lightweight nature, and adjustable conductivity[3]. These qualities render them ideally suited for use in modern electronics, where small size and effectiveness are crucial[4]. In addition, the capacity to customize the composition and structure of organic composites enables the creation of cutting-edge electronic devices that exhibit enhanced performance and longevity, while having reduced environmental footprint. Nevertheless, there is a wide range of organic materials available, and not all of them are suitable for use in electronics. However, the search for materials can be narrowed down by focusing on specific characteristics such as organic materials with a conjugated π-system and a strong electron-acceptor or electron-donor group. This material demonstrates a push-pull system (D–π–A) that enables efficient intermolecular charge transfer, resulting in low energy barriers[5].

The memory device industry is current working on replacing conventional silicon-based data storage devices such as flash, static random-access memory, and dynamic random-access memory by advanced memory technologies, including resistive random-access memory (ReRAM), phase-change memory, magnetic random-access memory, and others[6]. This is in an effort to optimize efficiency and enhance performance while minimizing energy consumption on these devices. ReRAMs remains the most attractive emerging memory among others, due to its excellent scalability ($< 10\ nm$), less power consumption (sub- pJ), high endurance ($> 10^{12}$ write/erase cycles)[7]. In a basic ReRAM cell, a specialized resistive switching material is positioned between two electrodes. An electrical potential is employed to switch between the two resistance states of a ReRAM cell, thereby turning on or off the device. These devices can function independently without requiring a control transistor. This makes ReRAMs to have the simple and efficient architecture leading to their growing popularity compared to other emerging memory devices. Recent research has demonstrated that ReRAM cells can be easily assembled to create synapses in artificial neural networks[8]. This enables the development of neuromorphic systems that closely imitate the functioning of biological brains[9]. Furthermore ReRAMs have been shown to be compatible with artificial intelligence, and the Internet of Things[10]. In recent reports, Kim et al. recently fabricated a biodegradable and flexible agarose-gold nanoparticle composite-based ReRAM. This system did not only show large memory $R_{ON}/R_{OFF} = 10^4$ and an endurance estimated as 10 year, but also an ability to emulate biological synapse with 64.4 $pJ/event$

and 164.4 $pJ/event$ potentiation and depression energy consumption, respectively[11]. This follows the observation of switching synaptic behaviour in ionic liquids[12]. In the present study, a biocomposite consisting of carboxymethyl cellulose (CMC) blended with methanol derived *Elaeodendron buchananii* plant extract (EBMeOH) was used as a resistive switching material in a device consisting of silver (Ag) and tungsten (W) electrodes. CMC is a watersoluble derivative of cellulose, an abundant, linear polysaccharide found in plants, algae, and the oomycetes. CMC is an anionic polymer, comprising $-CH_2COOH$ groups, which has found applications in various industries such as food packaging, agriculture, drug delivery, water treatment, and more[13–15].

Various polymers, including chitosan[16, 17], PVP[18], and more, have been utilized in their original state as well as in combination with other materials. A majority of these polymers are modified by dispersing nanoparticles. Nevertheless, the combination of two polymers has proven to be a viable method for enhancing the functionality of materials, while avoiding the use of metal particles that can pose environmental risks[19]. CMC and its composites have found utilization in various fields, including electronics. They have been utilized as electrolytes for energy storage devices [20], piezoresistive devices[21], sensing devices[22], and other applications[23, 24]. When combined with graphene oxide, the CMC nanocomposite has shown impressive results with a large R_{ON}/R_{OFF} ratio of 10^5, achieved at 2.22 V[25].

In addition to polymers, resistive switching has been observed in cow milk[26–28] and plant materials[29]. The majority of these materials already contain metallic ions as their inherent components. This is a benefit, as there is no requirement to introduce external nanoparticles to enhance electronic functionality. In this study, CMC was combined with methanol based *Elaeodendron buchananii* (EBMeOH) plant extract to create a biocomposite that exhibits resistive switching properties. This represents a novel method for enhancing the performance of polymers without the use of metallic nanoparticles.

2 Experimental Section

2.1 Extraction and device fabrication

2.1.1 Collection of plant material

The stem bark (Fig. 1 a) was obtained in September 2002 from Mabira woodland in Buikwe District, Uganda, situated between the districts of Jinja and Lugazi. Mr. Joseph Kavuma, a taxonomist, conducted species identification in the Makerere University Herbarium. This herbarium is managed by the Department of Plant Science, Microbiology and Biotechnology, which is part of the College of Natural Sciences at Makerere University. The Department of Plant Science, Microbiology and Biotechnology at Makerere University Herbarium received a voucher specimen of *Elaeodendron buchananii*. It was assigned the identification number EBKGt789.

2.1.2 Extraction of plant material.

The plant material was cut into smaller fragments and allowed to air dry for 30 days at room temperature. The powdered plant material (500 g) was consecutively extracted at room temperature for 72 hours with hexane, dichloromethane, ethyl acetate, methanol, and water (2.5 L). The extracts were concentrated to dryness under vacuum at 40 ^0C after being filtered through cotton wool. The extracts were further dried in a desiccator and refrigerated in tightly closed bottles for further analysis.

Extraction results: Hexane, dichloromethane, ethyl acetate, methanol and water was employed as extraction solvents. to extract plant material from *Elaeodendron buchananii*. A yellow extract (1.54%) was obtained from the hexane, an orange extract (11.21%) from the dichloromethane, a brown extract (5.07%) from the ethyl acetate, a dark brown extract (29.52%) from the methanol and a dark brown extract (22.14%) from the water upon concentration.

Tannin removal from the methanol extract: Solid phase extraction was used to remove tannins from a dried methanol extract of *Elaeodendron buchananii* stem bark (referred to as EBMeOH in this study). A large column was charged with polyamide gel (150 g) to which

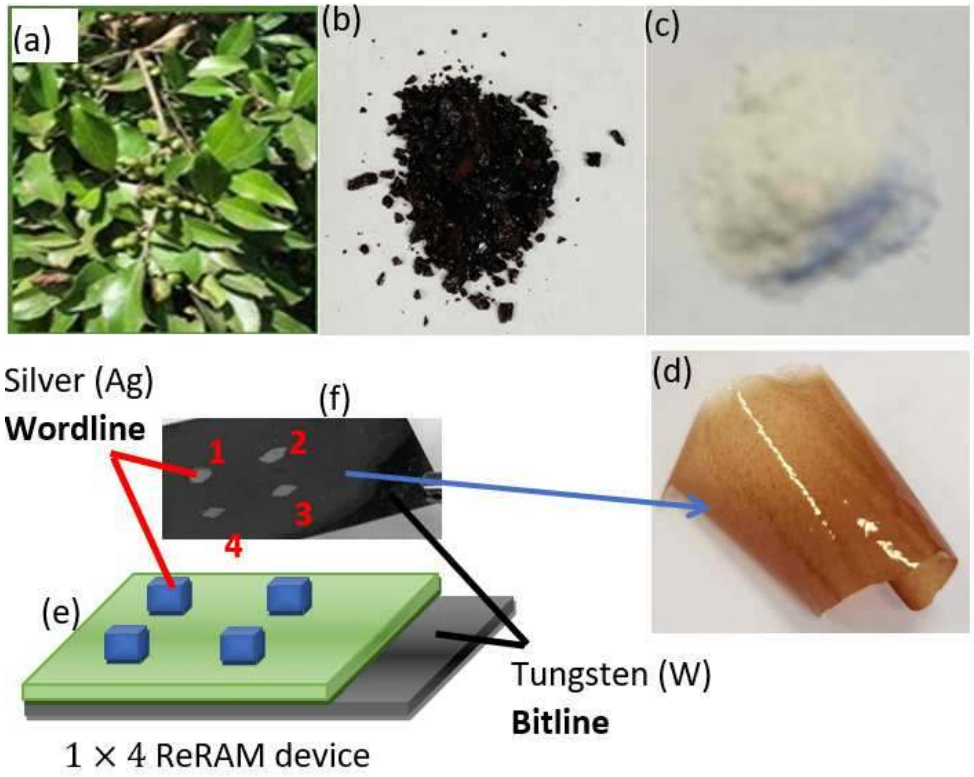

Fig. 1 Photographs of: (a) the AB trunk, (b) the EBMeOH extract, (c) the cmc powder, and (d) the free-standing ABMeOH-CMC film. (e) and (f) show a schematic design and image of a 1×4 Ag/EBMeOH-CMC/W ReRAM, respectively.

the reconstituted methanol extract was added (60.27 g in 1 L of methanol). Continuous additions of methanol were made to the column, until it was colorless, indicating that all the tannins from the extract had been eliminated. The eluant was concentrated to dryness under reduced pressure. The dried methanol extract (EBMeOH) (Fig. 1b) was weighed and stored in the fridge for further analysis.

2.1.3 ReRAM Device fabrication

EBMeOH (Fig. 1b) and CMC (Sigma Aldrich) (Fig. 1c) were dissolved in methanol to create two solutions with a weight percentage of 1%. Afterwards, the two solutions were combined and gently mixed to create a uniform EBMeOH-CMC composite solution. The tungsten (W) and polyethylene terephthalate coated with indium-doped tin oxide (PET-ITO) substrates underwent a meticulous cleaning process using sonication in isopropyl alcohol, methanol, and distilled water. A small quantity of EBMeOH-CMC solution was drop-casted onto both W and PET-ITO surfaces and allowed to air dry for 24 hours at room temperature. Unfortunately, the dried film on ITO lifted off and formed a standing EBMeOH-CMC film (Fig. 1d), thus making it impossible to prepare any device using this substrate. However, we successfully created a stable film on the W substrate, which enabled us to continue with the device fabrication process. In order to complete the device, a layer of silver (Ag) paste (Sigma Aldrich) was meticulously applied onto the surface of the film, resulting in the creation of four top electrodes. The device was left to air dry for additional 48 hours at room temperature. The device was built using the Ag/EBMeOH-CMC/W configuration, with Ag serving as the top electrode (TE) and W as the bottom electrode (BE). The device in question featured a single column and four rows, with designations of $B = 1$ and $W^* = 1, 2, 3$ & 4, where B and W^* represent bitline and wordline, respectively (here we decided to use W^* instead of W, as the symbol W has already been used earlier for tungsten). Therefore, the device

can be represented as a 1 × 4 Ag/ABMeOH-CMC/W ReRAM device. Figure 1(e and f) depict the schematic diagram and the photograph of the 1×4 Ag/ABMeOH-CMC/W ReRAM device fabricated in this study.

2.2 Characterization Techniques

2.2.1 ATR FTIR and Thermal Analysis

The functional groups of the compounds were examined by Attenuated Total Reflectance Fourier-transform infrared (ATR FTIR) spectroscopy (Bruker Tensor 27 model), analyzed with OPUS v1.1 software and fitted with a Pike single bounce diamond ATR crystal. For thermal decomposition and melting point determination, approximately 5 mg of the sample was weighed with a heating rate of 10 ℃/min. For Thermogravimetric analyses (TGA), the samples were analyzed on the Mettler-Toledo thermogravimetric analyzer (TGA/SDTA851) under a nitrogen atmosphere and the obtained thermograms were evaluated by STAR SW 8.10 software. Melting points were determined by differential scanning calorimetry (DSC). The analysis was performed using the DSC 5000 Discovery series equipement. The data was analysed with the TRIOS software.

2.2.2 X-ray photoelectron spectroscopy, SEM/EDS and AFM

X-ray Photoelectron Spectroscopy (XPS) was used to analyse the elemental composition of the samples. A PHI 5000 Versaprobe system having a monochromatic AlK X-ray source ($Al\ K\alpha$ = 1486.6 eV at 50 μm, 12.5 W, and 15 kV energy (97 X-ray beam) was used for measurements. A JEOL JSM-7800F Field emission scanning electron microscopy (FE-SEM) equipped with an Oxford Aztec energy dispersive X-ray spectroscopy was used to study morphology and elemental composition. The electron beam voltage was maintained at 5 kV.

2.2.3 Electrical characterization

In order to comprehend the memory behavior of the device, an electrical characterization was performed utilizing a specialized memristor characterization device available in-house. Throughout the measurements, the memory behavior of an individual cell was investigated. The initial set of measurements were acquired utilizing the $W = 1|B = 1$ configuration, where 1 bitline and 1 word-line were employed. Specifically, the W electrode was linked to the bitline address, while the Ag electrode 1 was connected to the word address line.

3 RESULTS AND DISCUSSION

3.1 Morphological characterisation: SEM/EDS and AFM

The surface morphology differences between EBMeOH, CMC, and EBMeOH-CMC film were investigated using scanning electron microscopy (Fig. 2:a-c) at 60 000 times magnification. EBMeOH ((Fig. 2a) exhibited a relatively homogeneous and smooth surface, with cracks evident in the film. The surface of the commercial CMC ((Fig. 2b) can be described as an uneven, irregular smear with occasionally occurring granular structures. The surface of the EBMeOH-CMC ((Fig. 2c) appears relatively smooth, presenting the same minuscule granular structures as CMC. Additionally, small blisters (ranging between 20–110 nm) and tearing of the film can also be observed.

The EDS measurements of EBMeOH, CMC, and EBMeOH-CMC film ((Fig. 3:a-c) detected the presence of mostly carbon and oxygen. In the EDS of EBMeOH trace amounts of potassium, chlorine, and magnesium was also observed. For CMC a substantial amount of sodium was detected, most likely due to the incorporation of sodium ions into the structure of the CMC. The EDS of the EBMeOH-CMC film is representative of a combination of the EBMeOH and CMC, with a considerable amount of sodium as well as trace amounts of potassium and chlorine. In addition, silicon was also detected. Iridium (Ir) is present in all three sample, since the samples were coated with Ir to improve conductivity and to reduce charging. An AFM was further utilized to observe the topography of the EBMeOH-CMC film (Fig. 3d and e). The results show a smooth surface with peaks and valleys measuring 440 nm in height. The estimated average roughness over the scanned area of 10 × 10 μm^2 was 48.72 nm. The line

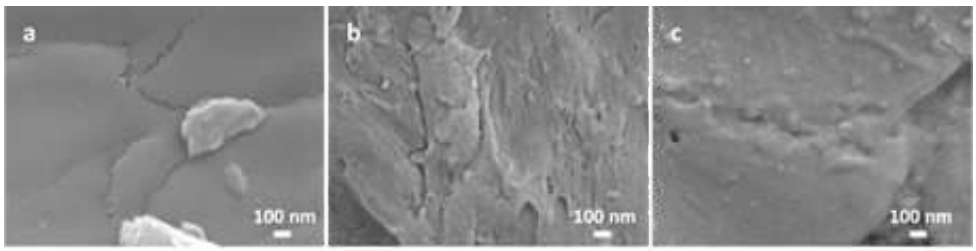

Fig. 2 SEM images of (a) EBMeOH, (b) CMC, and (c) EBMeOH-CMC film at 60 000 times magnification.

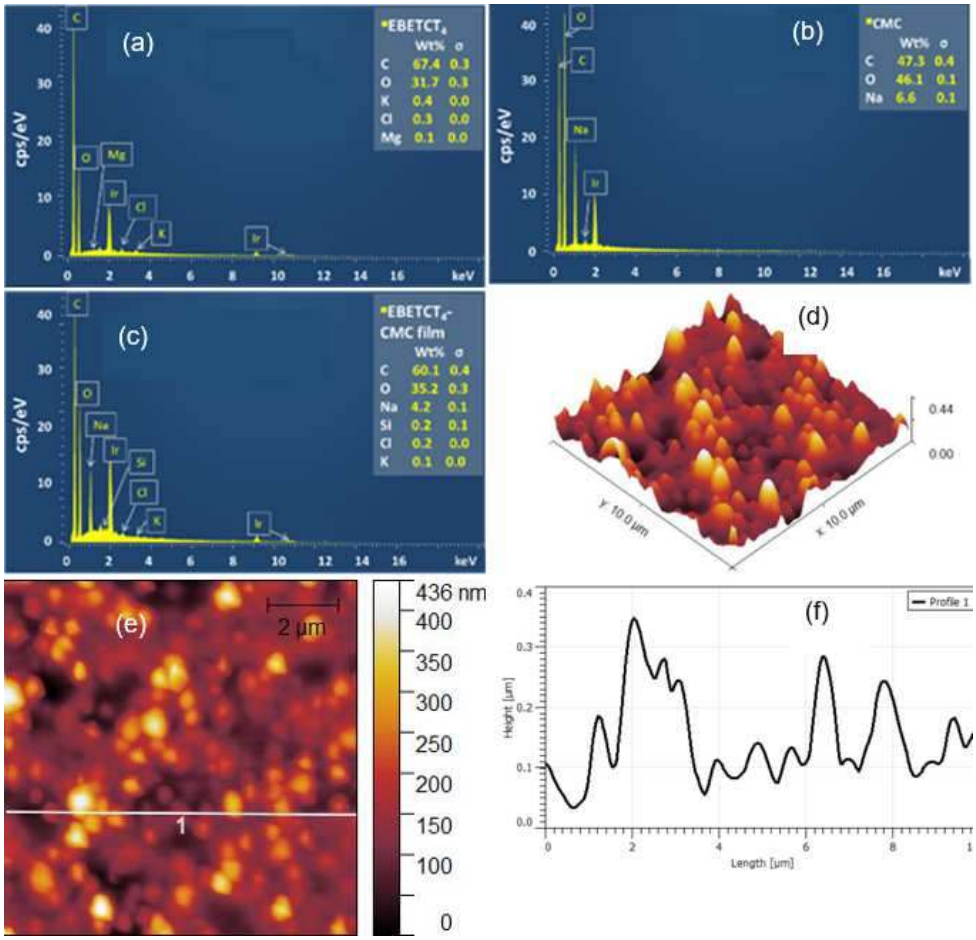

Fig. 3 EDS spectra of (a) EBMeOH, (b) CMC and (c) EBMeOH-CMC. AFM topography image of the EBMeOH-CMC in (d) 3D and (e) 2D, and the (f) surface line profile of the EBMeOH-CMC film.

profile (Profile 1) (Fig. 3f) shows an irregular surface variation. These findings are in line with the previously discussed SEM data.

3.1.1 XPS

X-ray Photoelectron Spectroscopy (XPS) was used to probe the core electronic properties of EBMeOH, CMC, and EBMeOH-CMC films. The survey scans (presented in the Supplementary Information) revealed the presence of carbon and oxygen in all the samples, with the addition of sodium in the CMC samples, thus confirming the EDS results. The photoelectron lines (C 1s, O 1s and Na 1s) of the samples were deconvoluted with simulated peaks to obtain the smallest possible

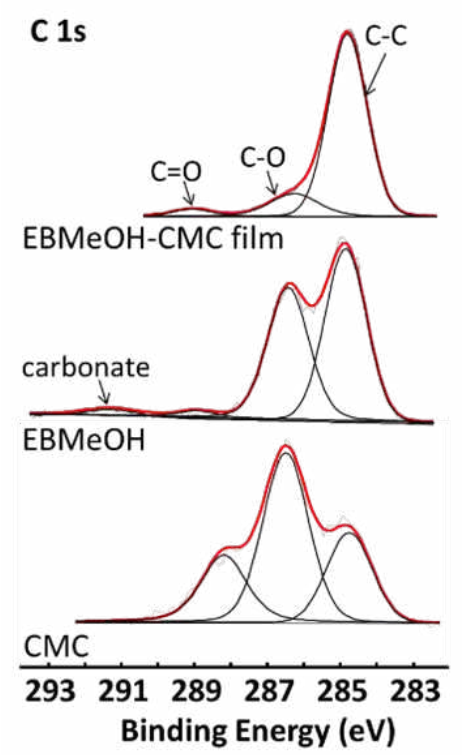

Fig. 4 The detail scan of the C 1s area of EBMeOH, CMC, and EBMeOH-CMC film. The red line represents the accumulated fitting of all the simulated peaks

CHISquare value. The peak at the lowest binding energy of the C 1s photoelectron line, representing the C-C (as well as C-H and adventitious carbon), was set at 284.8 eV for all the samples. The other forms of carbon present in the samples are C-O and C=O (see Fig. 4). EBMeOH show an additional photoelectron line at ca. 291 eV, which was assigned to carbonate groups, which could be present in plant extracts.

The data of the C 1s, O 1s, and Na 1s are summarised in Table 1. From the binding energy (BE) of the carbon one can deduce that the chemical environments of the C=O carbons in the EBMeOH and EBMeOH-CMC materials are similar. However, the BE of the C-O group drastically decreased with ca. 2 eV upon the addition of CMC. From this observation it can be assumed that the CMC forms a chemical bond with the C-O group in the EBMeOH potentially via the CO_2Na^+ site, causing the decrease in BE.

Table 1 XPS data of the C 1s, O 1s and Na 1s area, the carbon assignment, binding energy (BE) of the peak maximum and % present of the simulate fits.

	C is BE (eV)			Na 1s BE (eV)
Assignment	$C-C$	C-O	C=O	Na^+
CMC	284.8	286.5	288.2	1071.7
EBMeOH	284.8	287.4	288.8	-
EBMeOH-CMC	284.8	285.3	288.9	-

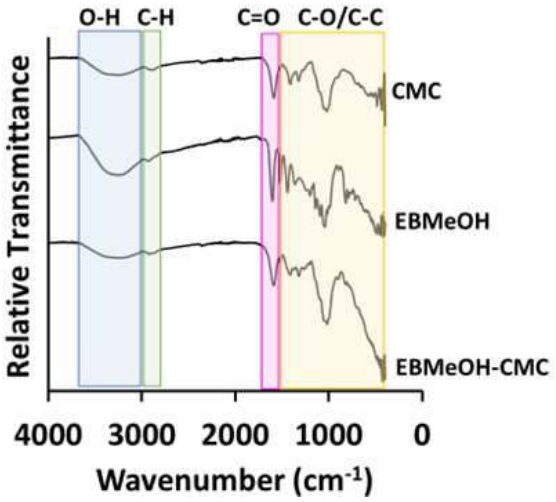

Fig. 5 The ATR FTIR spectra of CMC, EBMeOH and EBMeOH-CMC film composite.

Table 2 The stretching frequencies of the C-H, C=O and C-O bands as measured by ATR FTIR.

	C-H	C=O	C-O (ester/ ether)	C-O (primary alcohol)
CMC	2910/2871	1585	1320	1018
EBMeOH	2933/2848	1600	1364	1087
EBMeOH-CMC	2919/2849	1584	1318	1014

3.1.2 ATR FTIR

The ATR FTIR results are mutually consistent with the XPS, confirming the presence of functional groups, as well as the potential linking (association) via the C-O group of the EBMeOH to the CMC. The ATR FTIR of EBMeOH, CMC, and EBMeOH-CMC film are shown in Fig. 5 and

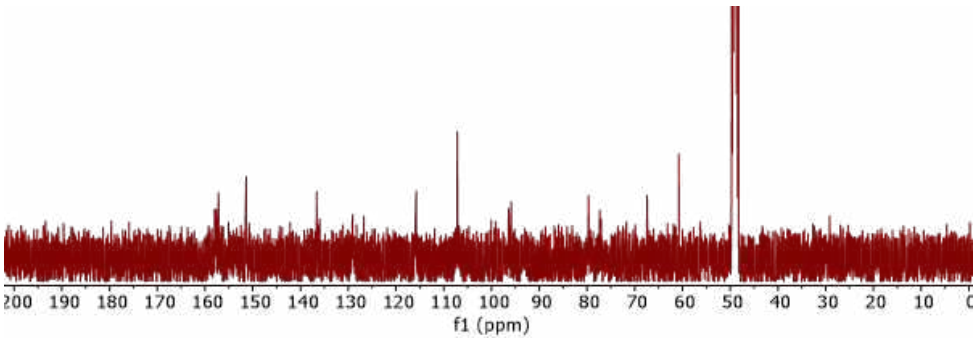

Fig. 6 ^{13}C NMR spectrum of EBMeOH in MeOD.

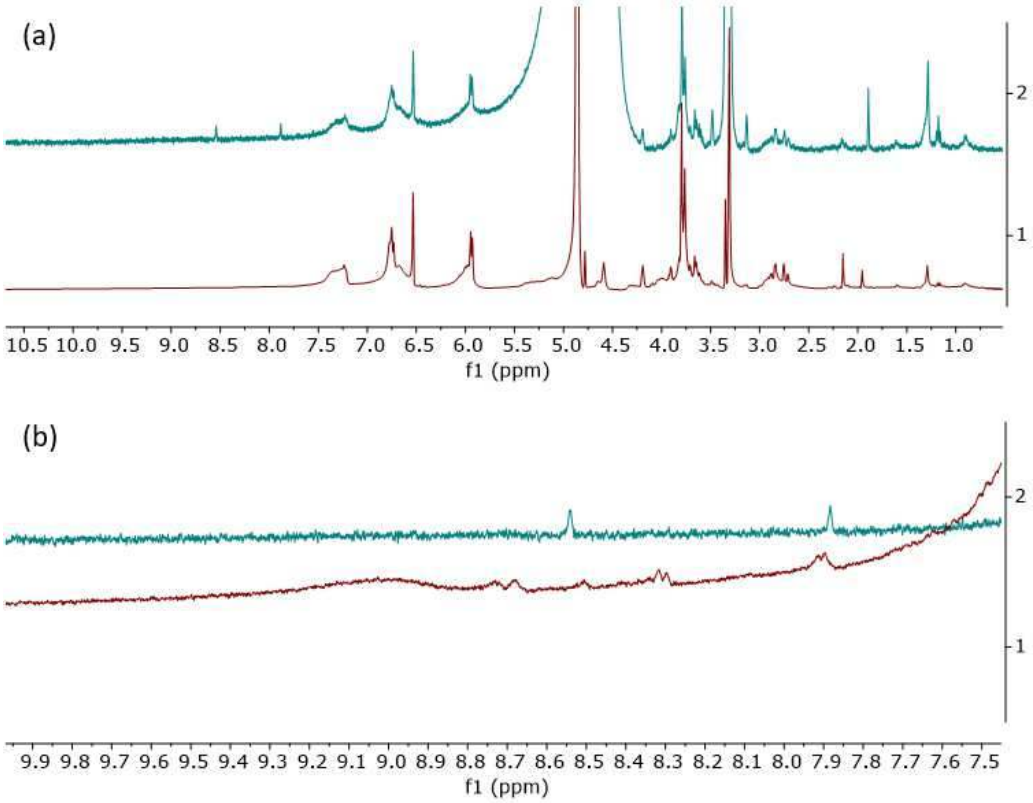

Fig. 7 (a) The ^1H NMR spectra of EBMeOH (1) and the EBMeOH-CMC adduct (2) in MeOD, and (b) the expansion of the -OH region of the ^1H NMR spectra for EBMeOH (1) and the EBMeOH-CMC adduct (2) in MeOD.

important data presented in Table 2. The symmetric and asymmetric stretching vibrations of the carboxylate groups (C=O) are represented by the bands at between 1400 and 1600 cm^{-1}. The two small band at ca. 2921 and 2856 cm^{-1} corresponds to C-H stretching. Within the range of $2900-3700$ cm^{-1}, a broad band is indicative of all the hydroxyl groups, attributed to the existence of both intermolecular and intramolecular hydrogen bonds. In the fingerprint region, numerous sharp and intense peaks are observed, signifying the C–O and C–C bending and stretching vibrations. The prominent band at 1040 cm^{-1} within the fingerprint region is attributed to the C-OH (primary alcohol group) stretching[30]. From the data in Table 2, there is a clear shift in the stretching frequencies of EBMeOH and EBMeOH-CMC film,

which implies that an chemical association/bond is formed between the EBMeOH and the CMC.

3.1.3 NMR

^{13}C Nuclear Magnetic Resonance (NMR) Spectroscopy further supported the presence of -OH and =O groups in the EBMeOH sample with resonances appearing in both the carbonyl (δ 150–180 ppm) and alcohol (δ 50–80 ppm) regions, respectively (Fig. 6). ^{1}H NMR confirmed that the structural backbone of EBMeOH remained unchanged even after the addition of CMC (Fig. 7a). Changes in the -OH region (δ 7.80–9.40 ppm) was however observed after the addition of CMC, confirming the potential bonding via the C-O group(s) of the EBMeOH to CMC (Fig. 7b).

3.1.4 Thermal decomposition

The thermal decomposition and melting characteristics of the sample were assessed by means of TGA and DSC. The thermogram revealed a two-step decomposition process for all compounds, as outlined in Table 3 and illustrated in Fig. 8. The initial decomposition, occurring between 39°C and 56°C, which is attributed to the removal of volatile solvent molecules such as water and methanol. The complete structural decomposition for all samples takes place at the temperatures exceeding 140 °C. Notably, pristine EBMeOH displays the lowest thermal stability, decomposing at 146 °C, while pristine CMC exhibits the highest stability at 279 °C. The inclusion of CMC in the plant extract to produce the film, resulted in significantly increased thermal stability of the composite. The decomposition temperature for the EBMeOH-CMC film is 187°C.

Table 3 The decomposition temperatures of the different steps and melting points of EBMeOH, CMC, and EBMeOH-CMC film.

Material	Decomposition temperature (^oC)		Melting point (^oC)
	Step 1	Step 1	
EBMeOH	39	146	111
CMC	56	279	121
EBMeOH-CMC	51	187	151

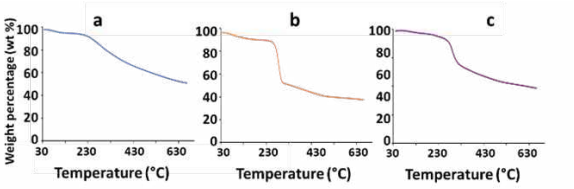

Fig. 8 The thermal decomposition profile of a) EBMeOH plant extract, b) carboxyethyl cellulose (CMC), and c) EBMeOH-CMC film.

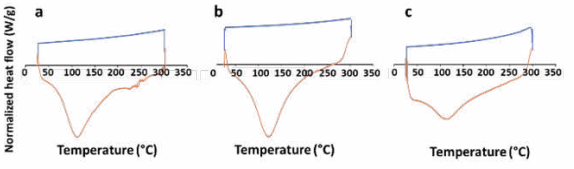

Fig. 9 The melting point profile of (a) EBMeOH, (b) CMC, and (c) EBMeOH-MC film.

3.1.5 Optical band gap energy

The solid-state UV-Vis absorption spectrum of the EBMeOH and EBMeOH-CMC film (see Fig. 10) were recorded, to determine their optical band-gap energy, at room temperature in the range of $250-800\ nm$. Though the optical band gap energy (E_g) does not a directly influence the resistive switching or memory properties of material, it is an indication of ease with which an electron in the valence band can be excited to the conduction band. This might give an indication of the proficiency of the material's resistive switching or memory properties. The optical band gap energies of EBMeOH and EBMeOH-CMC film were calculated from the absorbance vs wavelength graphs (Fig. 10), by using the Tauc's equation (Eq. 1):

$$(\alpha h\nu) = A(h\nu - E_g)^n \tag{1}$$

where α is an absorption coefficient, $h\nu$ is the photon's energy, A is the proportional constant,

Table 4 The optical band gap energies of EBMeOH, CMC and EBMeOH-CMC film.

	Optical bandgap energy (eV)		
CMC	3.93[a]	5.04[a]	-
EBMeOH	3.52	2.39	1.63
EBMeOH-CMC	4.01	-	-

[a] from Ref.[31]

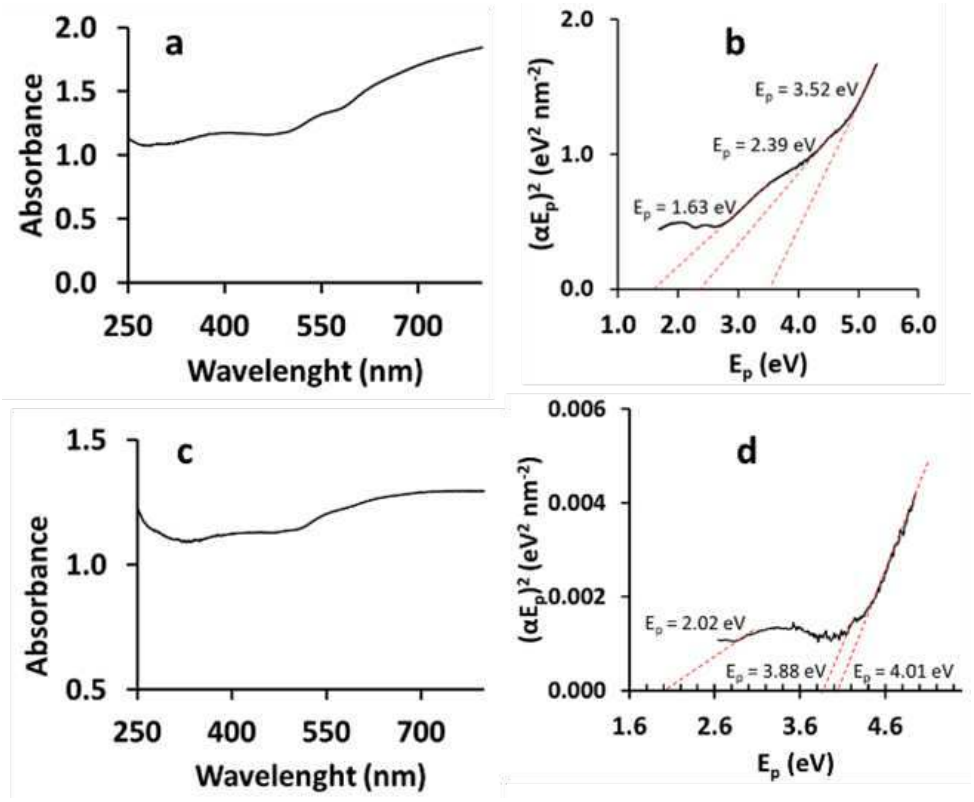

Fig. 10 (a) The UV-Vis spectra and (b) Tauc plot indicating the optical band gap energy of EBMeOH. (c) The UV-Vis spectra and (d) Tauc plot indicating the optical band gap energy of EBMeOH-CMC film.

E_g is the band gap energy and n denote the nature of the sample transition. The value of n for allowed direct, allowed indirect, forbidden direct and forbidden indirect transitions are 0.5, 2, 3/2, and 3[32]. This then allows the construction of a Tauc plot which shows a relationship between the absorption coefficient and optical band gap. The optical band gap of EBMeOH and EBMeOH-CMC film were determined by analyzing the energy value where the line intersects the x-axis. This was done by extrapolating the linear portion of the curves, as shown in Fig. 10. and the data summarized in Table 4.The addition of the CMC to the EBMeOH resulted in the material with slightly elevated (= 3.93 and 5.04 eV) optical band gap energies. This implies that the EBMeOH-CMC film needs more energy for the electrons to be excited than pristine EBMeOH.

3.1.6 Oxygen vacancy

The XPS of the O 1s photoelectron line was used to examine the oxygen vacancy of EBMeOH-CMC film. The O 1s photoelectron line of EBMeOH-CMC film is given in Fig. 11 and the data of the simulated peaks of CMC, EBMeOH, and EBMeOH-CMC film are summarised in Table 5. The broad O 1s photoelectron lines of all the samples were deconvoluted with four simulated lines. In correlation with literature[33], C=O (ca. 531.1 eV), C-O (ca. 532.2 eV), and C-O-C/O-H (ca. 533.9 eV), were assigned to the organic compound. In accordance with literature, the line at 533.1 eV could potentially be attributed to the binding energy of the oxygen vacancy[34].

3.2 Resistive switching characteristics

The $W^* = 1|B = 1$ cell was thoroughly characterized by conducting a series of staircase increasing pulses. The initial voltage was set at 0.05 V, with an increment step of 0.05 V and a step width of 50 ms. The interpulse time was set at 10 ms and a current compliance of 100 μA was used. The current-voltage (I-V) graphs in Fig. 12 clearly

Table 5 The oxygen assignment of the O 1s photoelectron lines of EBMeOH-CMC film.

Sample name	O 1s binding energy (eV) % present			
	C=O	C-O	O-vacancy	O-H
CMC	531.3/23.4	532.5/42.7	533.2/23.7	533.8/10.2
EBMeOH	532.0/6.8	533.1/55.3	533.6/26.0	534.3/11.9
EBMeOH-CMC film	531.2/12.2	532.2/55.7	533.1/20.6	533.9/11.6

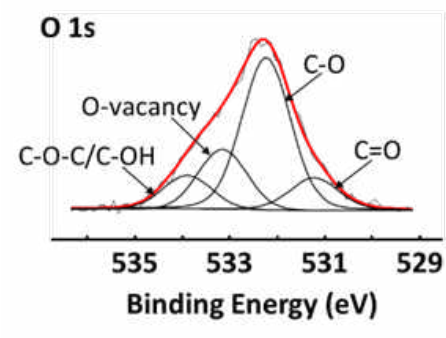

Fig. 11 Detail XPS of the O 1s area of EBMeOH-CMC film.

demonstrate that the current in the forward sweep and reverse sweep take different paths. This observation suggests that the $W^* = 1|B = 1$ cell possesses two distinct resistive states: the low resistive ON-state and the high resistive OFF-state. These resistive states are analogous to binary codes "1" and "0", for the ON- and OFF- states, respectively[6]. The amplitude of the voltage cycle was increased from 1 V (Fig. 12a), 2 V (Fig. 12b), 3 V, 4 V (Fig. 12c) and 5 V (Fig. 12d), and the hysteresis with relatively best R_{ON}/R_{OFF} ratio was observed at 4 V amplitude. In addition, during this increase in voltage scan amplitude, the device's resistive states undergo shifts in a way that result in the creation of wider hysteresis in the negative voltage bias (Fig. 12e). This demonstrates a voltage amplitude-dependent multiple resistive state, as depicted in (Fig. 12f). Multiple resistive states are an important characteristic feature for a device that can store multiple bits of data in a single cell. Voltage amplitude induced multiple resistive state has been reported before in DNA molecule-based ReRAM[35]. Not all systems exhibit multiple resistive states, and not all multiple states are induced by changing the voltage scan amplitude. In Ag/STO/Pt (STO is the $SrTiO_3$, and Pt is platinum) multiple resistive states were induced by changing the write voltage[36]. This was attributed to change in the size of the conductive filament (CF). Changing the I_{CC} is the most common way to induce multistate resistance as reported for the Ag/PMMA/$(BzA)_2CuBr_4$/Pt[37], Ag/$CH_3NH_3PbI_3$/Pt[38], and others [39].

The reliability study was performed by first running 1000 I-V scans at 4 V amplitude (Fig. 13). Our data analysis shows that there is no significant change in the I-V hysteresis, which indicates that the device has good endurance. The durability of the $W = 1|B = 1$ cell was further examined by applying alternating ± 1 V voltage pulses, each with a pulse width of 100 ms, to transition the cell from the OFF to the ON state, and vice versa. This protocol emulates the write and erase protocols executed in a computer system. For this protocol, the readings were taken at a voltage of 0.5 V, with a current compliance of 100 μA. As depicted in Fig. 14 8, our findings reveal clear resistive states, one in the OFF state and one in the ON state, with a resistance difference of approximately 2 megaohms. However, it is worth noting that there is considerable variation in the data for both states. Conducting a data retention study of the device was crucial in assessing its suitability as a nonvolatile memory. The retention data shown in Fig. 15 were obtained by applying a 1 V amplitude to select either the ON or OFF state. Once the state is selected, the resistance of the cell was read every 1 s. Our data shows that the resistance in both the ON and OFF states changes over time during the initial 800 s. After that, the resistance in both states remains constant, with some small data noise appearing in the ON state. Nevertheless, our findings indicate that data retention over time has significantly improved, making this cell a promising option for non-volatile memory applications.

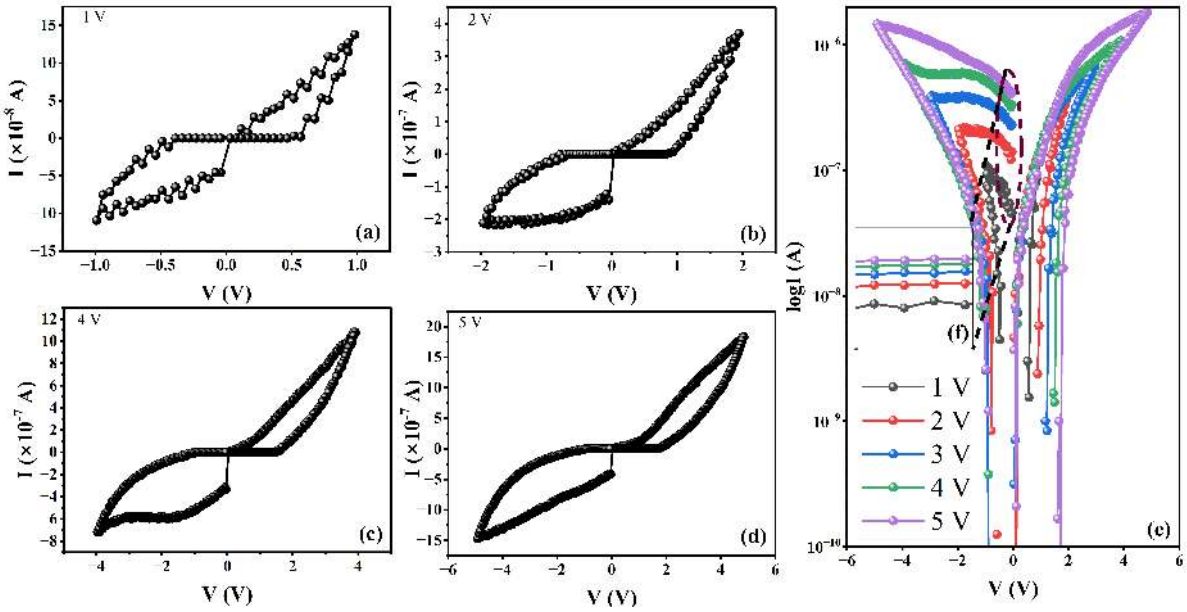

Fig. 12 The complete set of I-V graphs for the Ag/EBMeOH-CMC/W device, obtained at voltage amplitudes of 1 (a), 2 (b), 4 (c), and 5 (d) volts, while employing $W^* = 1|B = 1$ cell. Figure (e) depicts the amalgamated I-V graphs for the voltage scans ranging from 1 to 5 volts.

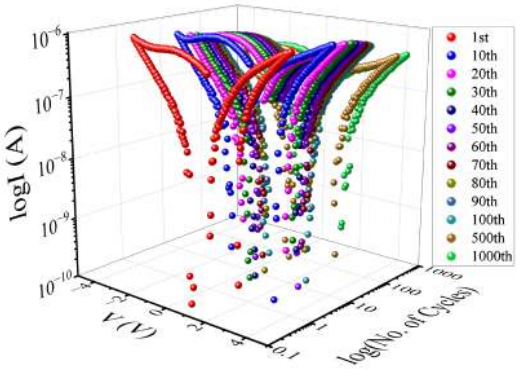

Fig. 13 The I-V graphs for the Ag/EBMeOH-CMC/W device, with a voltage amplitude of 4 V, were recorded for 1000 complete cycles. These measurements were taken specifically for the $W^* = 1|B = 1$ cell.

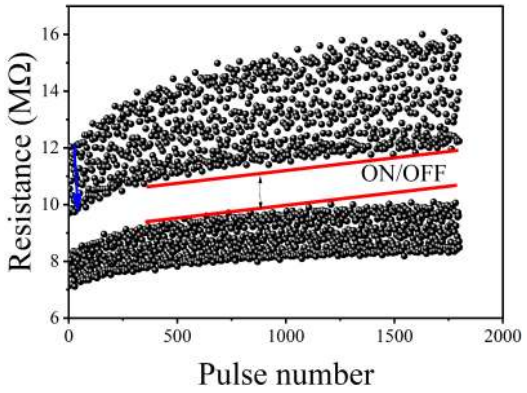

Fig. 14 The endurance performance for the $W^* = 1|B = 1$ cell of the Ag/ABMeOH-CMC/W Device measured during 1800 cycles. of

Finally, three additional memory cells were analyzed and the I-V data confirms consistent memory behavior. Here is the I-V variation of the $W = 4|B = 1$ cell for the first three voltage scan cycles, as shown in Figure 16. Based on our data analysis, it is evident that every cell in this device exhibits memory behavior. Consequently, this device can serve as a reliable storage medium for computer data.

3.2.1 Transport and switching mechanism analysis.

Figure 17(a-d) show the I-V variation of the device during the upwards ($0\ V \rightarrow 4\ V$) (red) and the downward ($4\ V \rightarrow 0\ V$) (black) voltage scans. From Fig. 17(a), we can observe that the flow of electric current only begins once the voltage reaches the threshold of 1.5 V. This might be due to high energy barrier at the electrode/composite interface, which must be overcome before

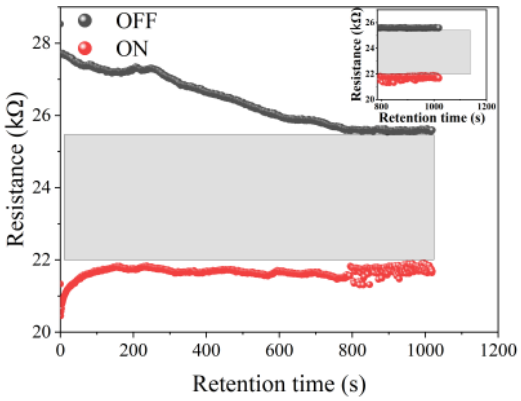

Fig. 15 Data retention of LRS and HRS performed at 1 V as read voltage for the $W = 1|B = 1$ cell of the Ag/ABMeOH-CMC/W Device.

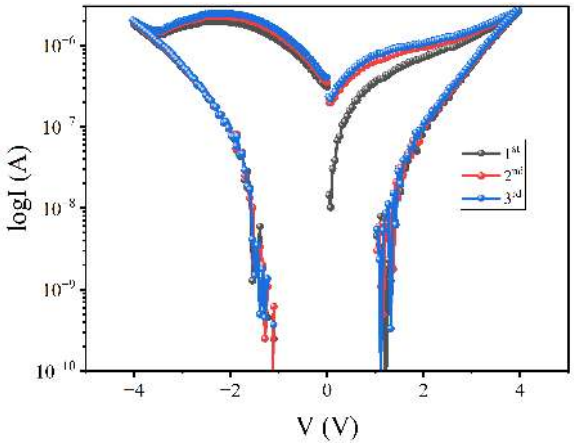

Fig. 16 The I-V graphs for the Ag/ABMeOH-CMC/W device, with a voltage amplitude of 4 V, were recorded for 3 complete cycles. These measurements were taken specifically for $W = 4|B = 1$ cell.

electrons can cross the interface into the composite. This is a well knows Schottky barrier height (Φ_B) which can be losely estimated as the difference in workfunction of the Ag or W electrode and the EBMeOH-CMC composite's electron affinity[40]. Shottky barrier effects have been reported in polymer-coposite based ReRAM (Ag/ PMMA@CsPbI3/FTO) device[41]. Increasing the voltage reduces the barrier height, and electrons finally penetrate the EBMeH-CMC composite, resulting in a current, as illustrated Fig 17(a). In this region, the I-V variation graph is not linear. Instead, it resembles a modest exponential trajectory, indicating hopping-type conduction. However, further confirmation of this hypothesis is required. When the voltage is decreased, the current appears to follow a more linear trajectory than in the preceding scenario. To further explore these two graphs, we rescaled them to log-log scale, as shown in Fig. 17(b). By analyzing the slope of the log-log plot, we can determine the value of n for the relationship $J \propto V^n$ (J is the current density and V is the applied voltage) and gain insights into the conduction mechanism in the composite. For the ON-state current, a linear fit was obtained with a value of $n = 1.45$, which is greater than $n = 1$ for the Ohmic case and less than $n = 2$ for the Child's square law[42]. For the OFF state, the graph only shows a linear I-V relationship at high voltage, with $n = 3$. After experimenting with various other mechanisms, the graph depicting the current in the OFF-state aligned perfectly with the trap-assisted tunneling (TAT) current model ($\ln J \propto -\frac{1}{V}$), as illustrated in Fig. 17(c). However, in the ON state, a linear region was only observed at higher voltage levels (Fig. 17d). In these linear regions, the slopes are $-8.8\ A.V$ (with uncertainty of $0.08\ A.V$) and $-2.74\ A.V$ (with uncertainty of $0.04\ A.V$), for the OFF- state and ON-states, respectively. The complete mathematical representation of the TAT conduction mechanism is as follows[42]:

$$J_{TAT} = A \exp -\frac{8\pi\sqrt{2qm^*}}{3hE}\phi_T^{3/2} \qquad (2)$$

where A is a constant, ϕ_T represents the trap energy level, which refers to the energy of the electron traps in relation to the conduction edge of the oxide. E denotes the applied electric field, m^* stands for the electron effective mass in the active layer, and h represents the Plank's constant[43].

In order to explain the TAT mechanism in the system under investigation, we hypothesized that initially, the electrons are unable to enter the EBMeOH-CMC composite due to the barrier energy at the Ag/EBMeOH-CMC and/or W/EBMeOH-CMC interface. As a result, no current is generated at low voltage. The EBMeOH-CMC system already contains oxygen, therefore it is anticipated that this system will exhibit typical oxide film behavior, as described by Funck et al[44]. Thus, as the voltage is raised, Oxygen vacancies (V_O^{2+}) are generated and accumulate in the vicinity of the electrode. This reduces the

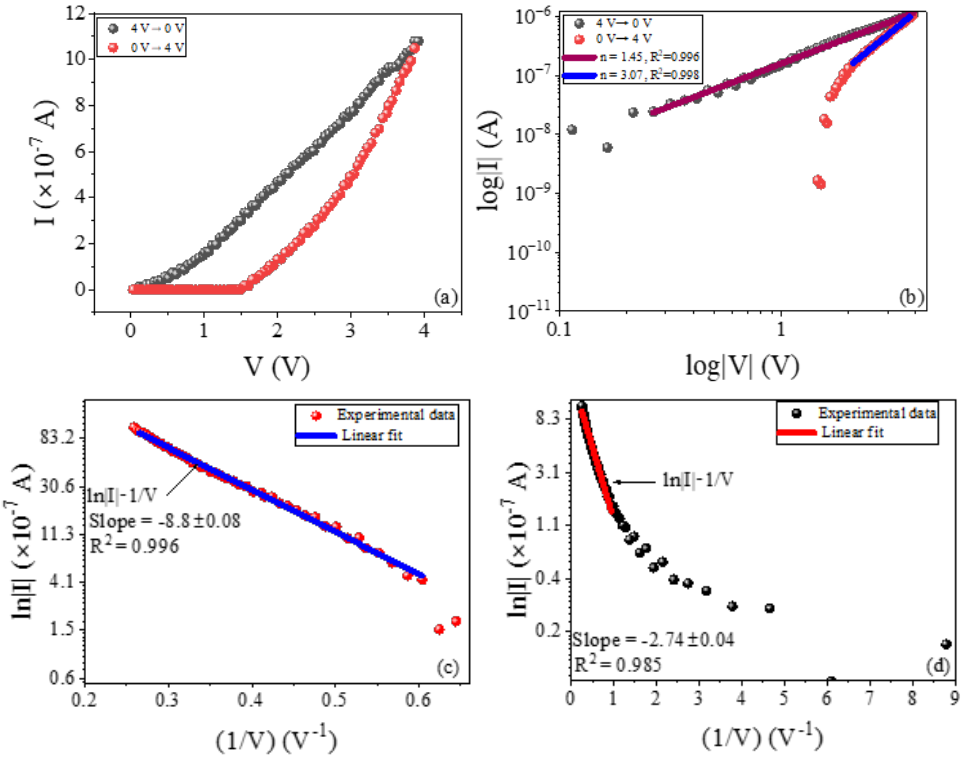

Fig. 17 The (a) linear and (b) log-log I-V variation graphs, as well as the trap-assisted tunneling graph for the (c) OFF- and (d) ON-states of the Ag/EBMeOH-CMC/W device.

energy barrier height at the interface, enabling electrons to penetrate the interface and resulting in the generation of current. Electrons are absorbed into the vacancies, which serve as trap sites in the Ag/EBMeOH-CMC/W system. This model's signature is the reemission of electrons from one trap site to the next, which can be attributed to various factors like thermal effects. This phenomenon occurs until electrons successfully travel to the opposite electrode. When the voltage is decreased, the current takes a specific path, indicating a low level of resistance. This phenomenon occurs due to the relationship between voltage and the number of defects. As the voltage increases, the number of defects also increases, resulting in an exponential I-V behavior. Interestingly, when the voltage is decreased, the system retains the last state characterized by a specific number of defects. Hence the system remain in a low resistive state. According to this hypothesis, the behaviour shown in Fig. 12 proves that the voltage amplitude influence the concentration of defects, resulting in varying states of conductance and the observed multistate switching. We also acknowledge that the W electrode is highly oxidizable and may also contribute to the observed switching behavior.

4 Conclusion

EBMeOH, a methanol-based extract of the *Elaeodendron buchananii* plant, was blended with carboxymethyl cellulose, a biopolymer, to create a biodegradable and eco-friendly functional material for resistive switching memory. This combination was tested in a device made up of silver and tungsten electrodes. Chemical and optical evaluation revealed that the two materials interacted, resulting in a composite with a larger optical band gap than the individual materials. Electrican analysis of the entire device revealed significant current-voltage hysteresis, which is typical of O-type memory behaviour, revealing a low ON/OFF ratio but strong durability and fair data retention. Furthermore, we discovered through transport mechanism analysis that the development of traps in the composite enhanced conduction in

the device, and that changing the voltage amplitude alters the concentration of traps, resulting in voltage amplitude driven multiple resistive states, necessary for multibit data storage and neuromorphic computing. Overall, our findings demonstrate that polymers can be functionalized by combining them with plant extracts to create novel materials for biodegradable nonvolatile memory devices.

Acknowledgements

This work is partially supported by BRICS grant BRIC2204203882, grant number 150501 and NRF grants ITAL2205015599, Grant number 150558 and SRUG2204305453

References

[1] Nur Amalina Binti Zulkifli, Muhammad Akmal Johar, Omar Mohd Faizan Marwah, and Mohd Halim Irwan Ibrahim. Review on Advances of Functional Material for Additive Manufacturing. *IOP Conference Series: Materials Science and Engineering*, 226(1), 2017. ISSN 1757899X. doi: 10.1088/1757-899X/226/1/012177.

[2] Sk Mahamuda, K. Swapna, M. Venkateswarlu, M. V.V.K. Srinivasa Prasad, and P. Sailaja. A review on applications of various functional materials. *International Journal of Scientific and Technology Research*, 9(1):3756–3759, 2020. ISSN 22778616.

[3] Lixia Li, Lijing Han, Haiqing Hu, and Ruoyu Zhang. A review on polymers and their composites for flexible electronics. *Materials Advances*, 4(3):726–746, 2022. ISSN 26335409. doi: 10.1039/d2ma00940d.

[4] Bingbin Wu, Habilou Ouro-Koura, Shao Hao Lu, Huidong Li, Xueju Wang, Jie Xiao, and Zhiqun Daniel Deng. Functional materials for powering and implementing next-generation miniature sensors. *Materials Today*, 69(October):333–354, 2023. ISSN 18734103. doi: 10.1016/j.mattod.2023.09.001. URL https://doi.org/10.1016/j.mattod.2023.09.001.

[5] Surajit Sarkar, Hritinava Banik, Farhana Yasmin Rahman, Swapan Majumdar, Debajyoti Bhattacharjee, and Syed Arshad Hussain. Effect of long chain fatty acids on the memory switching behavior of tetraindolyl derivatives. *RSC Advances*, 13(38):26330–26343, 2023. ISSN 20462069. doi: 10.1039/d3ra03869f. URL http://dx.doi.org/10.1039/D3RA03869F.

[6] Zolile Wiseman Dlamini, Sreedevi Vallabhapurapu, Olamide Abiodun Daramola, Potlaki Foster Tseki, Rui Werner Macedo Krause, Xavier Siwe-Noundou, Tebogo Sfiso Mahule, and Srinivasu Vijaya Vallabhapurapu. Resistive Switching in CdTe/CdSe Core–Shell Quantum Dots Embedded Chitosan-Based Memory Devices. *Journal of Circuits, Systems and Computers*, 31(06):1–16, 4 2022. ISSN 0218-1266. doi: 10.1142/S0218126622501134. URL https://www.worldscientific.com/doi/abs/10.1142/S0218126622501134.

[7] F. Pan, S. Gao, C. Chen, C. Song, and F. Zeng. Recent progress in resistive random access memories: Materials, switching mechanisms, and performance. *Materials Science and Engineering R: Reports*, 83(1):1–59, 2014. ISSN 0927796X. doi: 10.1016/j.mser.2014.06.002. URL http://dx.doi.org/10.1016/j.mser.2014.06.002.

[8] Daniele Ielmini. Brain-inspired computing with resistive switching memory (RRAM): Devices, synapses and neural networks. *Microelectronic Engineering*, 190:44–53, apr 2018. ISSN 01679317. doi: 10.1016/j.mee.2018.01.009.

[9] Meiran Zhao, Bin Gao, Jianshi Tang, He Qian, and Huaqiang Wu. Reliability of analog resistive switching memory for neuromorphic computing. *Applied Physics Reviews*, 7(1):011301, 3 2020. ISSN 1931-9401. doi: 10.1063/1.5124915. URL https://doi.org/10.1063/1.5124915.

[10] Jianjian Wang, Lanlong Ji, Jinshun Bi, Mengxin Liu, Kai Xi, Sandip Majumdar, and Safdar Mehmood. Design of RRAM

with high storage capacity and high reliability for IoT applications. *Solid-State Electronics*, 194(October 2021):108292, 2022. ISSN 00381101. doi: 10.1016/j.sse.2022.108292. URL https://doi.org/10.1016/j.sse.2022.108292.

[11] Youngjin Kim, Jun Seop An, Donghee Lee, Seong Yeon Ryu, Yoon Chul Hwang, Dae Hun Kim, and Tae Whan Kim. Biocompatible memristive device based on an agarose@gold nanoparticle-nanocomposite layer obtained from nature for neuromorphic computing. *Scientific reports*, 13(1):6491, 2023. ISSN 20452322. doi: 10.1038/s41598-023-32860-6. URL https://doi.org/10.1038/s41598-023-32860-6.

[12] Muhammad Umair Khan, Jungmin Kim, Mahesh Y Chougale, Chaudhry Muhammad Furqan, Qazi Muhammad Saqib, Rayyan Ali Shaukat, Nobuhiko P Kobayashi, Baker Mohammad, Jinho Bae, and Hoi-sing Kwok. Ionic liquid multistate resistive switching characteristics in two terminal soft and flexible discrete channels for neuromorphic computing. *Microsystems Nanoengineering*, 8(1):56, may 2022. ISSN 2055-7434. doi: 10.1038/s41378-022-00390-2. URL https://www.nature.com/articles/s41378-022-00390-2.

[13] Md Saifur Rahman, Md Saif Hasan, Ashis Sutradhar Nitai, Sunghyun Nam, Aneek Krishna Karmakar, Md Shameem Ahsan, Muhammad J.A. Shiddiky, and Mohammad Boshir Ahmed. Recent developments of carboxymethyl cellulose. *Polymers*, 13(8), 2021. ISSN 20734360. doi: 10.3390/polym13081345.

[14] Vishal Tyagi and Archana Thakur. Applications of biodegradable carboxymethyl cellulose-based composites. *Results in Materials*, 20(November):100481, 2023. ISSN 2590048X. doi: 10.1016/j.rinma.2023.100481. URL https://doi.org/10.1016/j.rinma.2023.100481.

[15] Warinporn Klunklin, Kittisak Jantanasakulwong, Yuthana Phimolsiripol, Noppol Leksawasdi, Phisit Seesuriyachan, Thanongsak Chaiyaso, Chayatip Insomphun, Suphat Phongthai, Pensak Jantrawut, Sarana Rose Sommano, Winita Punyodom, Alissara Reungsang, Thi Minh Phuong Ngo, and Pornchai Rachtanapun. Synthesis, Characterization, and Application of Carboxymethyl Cellulose from Asparagus Stalk End. *Polymers*, 13(1):81, dec 2020. ISSN 2073-4360. doi: 10.3390/polym13010081. URL https://www.mdpi.com/2073-4360/13/1/81.

[16] Zolile Wiseman Dlamini, Sreedevi Vallabhapurapu, Olamide Abiodan Daramola, Potlaki Foster Tseki, Rui Werner Macedo Krause, Xavier Siwe-Noundou, Tebogo Sfiso Mahule, and Srinivasu Vijaya Vallabhapurapu. Conduction and Resistive Switching in Dropcast CdTe/CdSe Core-Shell Quantum Dots Embedded Chitosan Composite. *Iranian Journal of Science and Technology, Transactions A: Science*, 46(2):709–716, 4 2022. ISSN 1028-6276. doi: 10.1007/s40995-022-01272-y. URL https://doi.org/10.1007/s40995-022-01272-yhttps://link.springer.com/10.1007/s40995-022-01272-y.

[17] Coplanar Nanogap Electrodes, Niloufar Raeis-hosseini, Dimitra G Georgiadou, and Christos Papavassiliou. High On / Off Ratio Carbon Quantum Dot – Chitosan Biomemristors with High On / Off Ratio Carbon Quantum Dot Chitosan Biomemristors with Coplanar Nanogap Electrodes. (December), 2022. doi: 10.1021/acsaelm.2c00979.

[18] Z.W. Dlamini, S Vallabhapurapu, A Srinivasan, S. Wu, and V.S. Vallabhapurapu. Resistive Switching in Polyvinylpyrrolidone/-Molybdenum Disulfide Composite-Based Memory Devices. *Acta Physica Polonica A*, 141(5):439–444, 5 2022. ISSN 1898-794X. doi: 10.12693/APhysPolA.141.439. URL http://przyrbwn.icm.edu.pl/APP/PDF/141/app141z5p01.pdf.

[19] Zolile Wiseman Dlamini, Sreedevi Vallabhapurapu, Shuying Wu, Tebogo Sfiso Mahule, Ananthakrishnan Srivivasan, and Vijaya Srinivasu Vallabhapurapu.

Resistive switching memory based on chitosan/polyvinylpyrrolidone blend as active layers. *Solid State Communications*, 345:114677, apr 2022. ISSN 00381098. doi: 10.1016/j.ssc.2022.114677. URL https://linkinghub.elsevier.com/retrieve/pii/S0038109822000254.

[20] Maida Akhlaq, Umair Mushtaq, Sadia Naz, and Maliha Uroos. Carboxymethyl cellulose-based materials as an alternative source for sustainable electrochemical devices: a review. *RSC Advances*, 13(9):5723–5743, 2023. ISSN 20462069. doi: 10.1039/d2ra08244f.

[21] Van At Nguyen, Mariam Odetallah, Gorkem Bakir, Kathleen Gough, and Christian Kuss. Piezoresistive Behavior of Polypyrrole:Carboxymethyl Cellulose Composites. *ACS Omega*, 7(46):41937–41942, 2022. ISSN 24701343. doi: 10.1021/acsomega.2c03461.

[22] R. Barras, I. Cunha, D. Gaspar, E. Fortunato, R. Martins, and L. Pereira. Printable cellulose-based electroconductive composites for sensing elements in paper electronics. *Flexible and Printed Electronics*, 2(1), 2017. ISSN 20588585. doi: 10.1088/2058-8585/aa5ef9.

[23] Laila M. Al-Harbi, Qana A. Alsulami, M. O. Farea, and A. Rajeh. Tuning optical, dielectric, and electrical properties of Polyethylene oxide/Carboxymethyl cellulose doped with mixed metal oxide nanoparticles for flexible electronic devices. *Journal of Molecular Structure*, 1272:134244, 2023. ISSN 00222860. doi: 10.1016/j.molstruc.2022.134244. URL https://doi.org/10.1016/j.molstruc.2022.134244.

[24] Yanan Wang, Hanyu Zhao, Lijie Huang, Guangxue Chen, Zhehao Wei, Qi Mo, Yishan Li, Xiyue Wang, Chongxing Huang, and Qifeng Chen. Development of chlorine dioxide sustained-release device using carboxymethyl cellulose-polyvinyl alcohol-β-cyclodextrin ternary hydrogel and a new sustained-release kinetic model. *Cellulose*, 30 (5):3073–3082, 2023. ISSN 1572882X. doi: 10.1007/s10570-023-05070-6.

[25] Tao Liu, Wei Wu, Kai Ning Liao, Qijun Sun, Xianjing Gong, Vellaisamy A.L. Roy, Zhong Zhen Yu, and Robert K.Y. Li. Fabrication of carboxymethyl cellulose and graphene oxide bio-nanocomposites for flexible nonvolatile resistive switching memory devices. *Carbohydrate Polymers*, 214(March): 213–220, 2019. ISSN 01448617. doi: 10.1016/j.carbpol.2019.03.040. URL https://doi.org/10.1016/j.carbpol.2019.03.040.

[26] Z. W. Dlamini, S. Vallabhapurapu, T. S. Mahule, and V. S. Vallabhapurapu. Electrical conduction and resistive switching in cow milk-based devices prepared using the spin-coat method. *AIP Adv.*, 12(9):095321, 2022. doi: 10.1063/5.0098976. URL https://doi.org/10.1063/5.0098976.

[27] Zolile Wiseman Dlamini, Sreedevi Vallabhapurapu, and Vijaya Srinivasu Vallabhapurapu. Resistive Switching Property of Raw Organic Cow Milk for Memory Application. *Sustainability*, 15(10):8250, may 2023. ISSN 2071-1050. doi: 10.3390/su15108250. URL https://www.mdpi.com/2071-1050/15/10/8250.

[28] Zolile Wiseman Dlamini, Wendy Setlalentoa, Sreedevi Vallabhapurapu, Tebogo Sfiso Mahule, Vijaya Srinivasu Vallabhapurapu, Olamide Abiodun Daramola, Potlaki Foster Tseki, Xavier Siwe-nondou, and Rui Werner Maçedo Krause. Resistive Switching Properties of CdTe/CdSe Core-Shell Quantum Dots incorporated Organic Cow Milk for Memory Application. *Functional Materials Letters*, 2023. doi: 10.1142/S1793604723400271. URL https://doi.org/10.1142/S1793604723400271.

[29] Z W Dlamini, S Vallabhapurapu, J Nambooze, A Wilhelm, E Erasmus, and M R Swart. Extraction , chemical , and dual-functional memory and threshold resistive switching characteristics of Elaeodendron buchananii extract. *Materials Today Communications*, 37(May):107159, 2023. ISSN 2352-4928. doi: 10.1016/j.mtcomm.2023.107159. URL https://doi.org/10.1016/j.mtcomm.2023.107159.

[30] Tehseen Riaz, Rabia Zeeshan, Faiza Zarif, Kanwal Ilyas, Nawshad Muhammad, Sher Zaman Safi, Abdur Rahim, Syed A. A. Rizvi, and Ihtesham Ur Rehman. FTIR analysis of natural and synthetic collagen. *Applied Spectroscopy Reviews*, 53 (9):703–746, oct 2018. ISSN 0570-4928. doi: 10.1080/05704928.2018.1426595. URL https://www.tandfonline.com/doi/full/10.1080/05704928.2018.1426595.

[31] Amina Omar, Rania Badry, Maroof A. Hegazy, Ibrahim S. Yahia, Hanan Elhaes, Heba Y. Zahran, Medhat A. Ibrahim, and Ahmed Refaat. Enhancing the optical properties of chitosan, carboxymethyl cellulose, sodium alginate modified with nano metal oxide and graphene oxide. *Optical and Quantum Electronics*, 54(12):806, dec 2022. ISSN 0306-8919. doi: 10.1007/s11082-022-04107-7. URL https://doi.org/10.1007/s11082-022-04107-7https://link.springer.com/10.1007/s11082-022-04107-7.

[32] J. Tauc, R. Grigorovici, and A. Vancu. Optical Properties and Electronic Structure of Amorphous Germanium. *physica status solidi (b)*, 15(2):627–637, jan 1966. ISSN 0370-1972. doi: 10.1002/pssb.19660150224. URL https://onlinelibrary.wiley.com/doi/10.1002/pssb.19660150224.

[33] Matthew Smith, Louis Scudiero, Juan Espinal, Jean-Sabin McEwen, and Manuel Garcia-Perez. Improving the deconvolution and interpretation of XPS spectra from chars by ab initio calculations. *Carbon*, 110:155–171, dec 2016. ISSN 00086223. doi: 10.1016/j.carbon.2016.09.012. URL https://linkinghub.elsevier.com/retrieve/pii/S0008622316307631.

[34] Minh Trung Dang, Josianne Lefebvre, and James D. Wuest. Recycling Indium Tin Oxide (ITO) Electrodes Used in Thin-Film Devices with Adjacent Hole-Transport Layers of Metal Oxides. *ACS Sustainable Chemistry Engineering*, 3 (12):3373–3381, dec 2015. ISSN 2168-0485. doi: 10.1021/acssuschemeng.5b01080. URL https://pubs.acs.org/doi/10.1021/acssuschemeng.5b01080.

[35] Shuchao Qin, Ruixin Dong, Xunling Yan, and Qianqian Du. A reproducible write-(read)n-erase and multilevel bio-memristor based on DNA molecule. *Organic Electronics*, 22:147–153, 2015. ISSN 15661199. doi: 10.1016/j.orgel.2015.03.045. URL http://dx.doi.org/10.1016/j.orgel.2015.03.045.

[36] Pengfei Hou, Zhanzhan Gao, and Kaikai Ni. Multilevel data storage memory based on polycrystalline SrTiO3 ultrathin film. *RSC Advances*, 7(78):49753–49758, 2017. ISSN 20462069. doi: 10.1039/c7ra09806e.

[37] So Yeon Kim, June Mo Yang, Eun Suk Choi, and Nam Gyu Park. Layered (C6H5CH2NH3)2CuBr4 Perovskite for Multilevel Storage Resistive Switching Memory. *Advanced Functional Materials*, 30(27):1–9, 7 2020. ISSN 16163028. doi: 10.1002/adfm.202002653.

[38] Jaeho Choi, Sunghak Park, Joohee Lee, Kootak Hong, Do-Hong Kim, Cheon Woo Moon, Gyeong Do Park, Junmin Suh, Jinyeon Hwang, Soo Young Kim, Hyun Suk Jung, Nam-Gyu Park, Seungwu Han, Ki Tae Nam, and Ho Won Jang. Organolead Halide Perovskites for Low Operating Voltage Multilevel Resistive Switching. *Advanced Materials*, 28(31):6562–6567, 8 2016. ISSN 09359648. doi: 10.1002/adma.201600859. URL https://onlinelibrary.wiley.com/doi/10.1002/adma.201600859.

[39] Muhammad Ismail, Chandreswar Mahata, and Sungjun Kim. Forming-free Pt/Al2O3/HfO2/HfAlOx/TiN memristor with controllable multilevel resistive switching and neuromorphic characteristics for artificial synapse. *Journal of Alloys and Compounds*, 892:162141, 2022. ISSN 09258388. doi: 10.1016/j.jallcom.2021.162141. URL https://doi.org/10.1016/j.jallcom.2021.162141.

[40] Muhammad Ismail, Zahida Batool, Khalid Mahmood, Anwar Manzoor Rana, Byung-Do Do Yang, and Sungjun Kim. Resistive

switching characteristics and mechanism of bilayer HfO2/ZrO2 structure deposited by radio-frequency sputtering for nonvolatile memory. *Results in Physics*, 18(April):103275, 9 2020. ISSN 22113797. doi: 10.1016/j.rinp.2020.103275. URL https://linkinghub.elsevier.com/retrieve/pii/S2211379720317423https://doi.org/10.1016/j.rinp.2020.103275.

[41] Jia Xu, Yanhong Wu, Zhenzhen Li, Xiaolong Liu, Guozhong Cao, and Jianxi Yao. Resistive Switching in Nonperovskite-Phase CsPbI3 Film-Based Memory Devices. *ACS Applied Materials and Interfaces*, 12(8):9409–9420, 2020. ISSN 19448252. doi: 10.1021/acsami.9b17680.

[42] Rohana Perera, Akihiro Ikeda, Reiji Hattori, and Yukinori Kuroki. Trap assisted leakage current conduction in thin silicon oxynitride films grown by rapid thermal oxidation combined microwave excited plasma nitridation. *Microelectronic Engineering*, 65 (4):357–370, 2003. ISSN 01679317. doi: 10.1016/S0167-9317(02)01025-0.

[43] Ee Wah Lim and Razali Ismail. Conduction mechanism of valence change resistive switching memory: A survey. *Electronics (Switzerland)*, 4(3): 586–613, 9 2015. ISSN 20799292. doi: 10.3390/electronics4030586. URL www.mdpi.com/journal/electronicshttp://www.mdpi.com/2079-9292/4/3/586.

[44] Carsten Funck and Stephan Menzel. Comprehensive Model of Electron Conduction in Oxide-Based Memristive Devices. *ACS Applied Electronic Materials*, 3(9):3674–3692, sep 2021. ISSN 2637-6113. doi: 10.1021/acsaelm.1c00398. URL https://pubs.acs.org/doi/10.1021/acsaelm.1c00398.